



Cyclic loading of a SiC-fiber reinforced ceramic matrix composite reveals damage mechanisms and thermal residual stress state

Konstantinos G. Dassios*, Dimitris G. Aggelis, Evangelos Z. Kordatos, Theodore E. Matikas

Department of Materials Science and Engineering, University of Ioannina, Ioannina GR-45110, Greece

ARTICLE INFO

Article history:

Received 25 May 2012

Received in revised form 5 June 2012

Accepted 23 June 2012

Available online 16 August 2012

Keywords:

A. Ceramic–matrix composites (CMCs)

B. Residual/internal stress

D. Mechanical testing

Acoustic emission

ABSTRACT

This study reports on the effects of axial thermal residual stresses, cyclic loading and presence of notches on the tensile performance of a SiC-fiber-reinforced barium–magnesium–alumina–silicate (BMAS) ceramic matrix composite. The residual stress state of the composite was experimentally measured by interrogation of the tensile curves at a uniquely well-defined common intersection point of unloading–reloading cycles in the tensile domain. Notch presence was critical on the material's mechanical response and promoted catastrophic failure shortly after the achievement of a saturated matrix crack state. The result of cyclic loading was an increase by 20% in sustainable stress throughout loading, as compared to pure tension. Scatter in elastic properties within specimens of different notch-to-width ratios was reconciled with theoretical expectations by application of a translation vector approach in the stress–strain plane, based on the material's residual stress state. Acoustic emission and infrared thermography provided valuable insight into damage identification, location and sequence.

© 2012 Elsevier Ltd. All rights reserved.

1. Introduction

The development of Continuous Fiber-reinforced Ceramic matrix Composites (CFCCs) with weak interfacial bonds, in the 1990s, led to great improvements to the intrinsic problems of brittleness, low fracture toughness and catastrophic failure of the otherwise continuous monolithic constituents. CFCCs are used today in various high-temperature applications with increased thermo-mechanical performance demands such as structural materials for aerospace industry, internal chambers and nozzles of jet motors, turbine nozzles, aircraft brakes, burner nozzles and thermal barriers. The mechanical performance of CFCCs depends on the constituents' properties, such as elastic moduli and strength, on fiber diameter and volume fraction, on the interfacial shear strength, and on the residual stress state of the composite. Thermal residual stresses (TRS) develop during fabrication of composite materials, upon cooling from high to ambient temperature, due to the mismatch of coefficients of thermal expansion (CTE) between the fiber and the matrix. These stresses can affect fiber/matrix interface conditions as they can induce matrix micro-cracks. Under such conditions, the establishment of accurate mechanical data is equally indispensable for modelling approaches as well as for design of structural applications of such composites.

During the last two decades, several methodologies have been reported for the experimental determination of the TRS of CFCCs,

usually through the assessment of the stress–strain behavior of the material in unloading/reloading tests and the phenomena of permanent strain accumulation and loop shape hysteresis observed therein [1–5]. Steen [3] and Camus [4] have shown that the coordinates of the common intersection point (CIP) formed by the compliance slopes of reloading–unloading loops, are directly related to the axial TRS of the composite. Mei et al. [6] recently proved the existence of the common intersection point by calculating the intersection points of 55 lines based on his 11 reloading–unloading cycles. The established residual stress value was successfully validated across its theoretically-predicted counterpart. The CIP approach is currently the only plausible method for evaluating TRS from mechanical test data.

This work is concerned with the establishment of the mechanical behaviour of a continuous SiC-fiber reinforced barium osumilite ($\text{BaMg}_2\text{Al}_6\text{Si}_9\text{O}_{30}$, BMAS:barium–magnesium–alumina–silicate) glass–ceramic matrix composite under cyclic tensile loading, the determination of the material's residual stress state and its effect on the material's elastic properties. The double-edge notch (DEN) specimen configuration with variable notch-to-width ratios was employed in order to (a) confine material damage within a pre-determined region, monitored by acoustic emission (AE) and infrared thermography (IRT) and (b) to evaluate the effect of notches on the mechanical response of the material. Unloading–reloading cycles were included during testing as an instantaneous probe of the composite's damage state AE waveform parameters such as the frequency with maximum amplitude within the spectrum (peak frequency, PF) provide information about the damage

* Corresponding author. Tel.: +30 26501 09010.

E-mail address: kdassios@cc.uoi.gr (K.G. Dassios).

condition of the material, and the extent of failure mechanisms such matrix cracking, fiber failure, delamination and pull-out [7–9]. IRT, on the other hand, is a powerful nondestructive evaluation tool that captures the development of damage mechanisms in the material, especially crack formation and propagation in different materials like concrete [10,11], metals [12,13] and metal matrix composites [13,14] under static or cyclic loading conditions [15]. The non-contact method offers wide area detection of subsurface damage activity, and can be used as an alternative or complement to conventional inspection technologies [16].

It was found that the imposition of cyclic loading resulted in an apparent material strengthening with respect to pure tension, with the envelope of the cyclic tension curves appearing at 20% higher stresses than those of pure tension. A very similar finding has been reported by Mei et al. in [17], where short-term pre-fatigue led to an increase by 23.47% in the strength of C/SiC composites. A “triple regime” behaviour was noted for un-notched specimens: the elastic regime was followed by a softening effect attributed to interfacial debonding while stiffening and increase in modulus due to load-bearing by intact fibers in a completely cracked matrix was characteristic in the final, pre-fracture, regime. Specimens with pre-fabricated notches did not exhibit this latter regime and failed soon after a saturated matrix crack state was achieved. The TRS state of the composite was evaluated directly from the tensile stress–strain curves of un-notched specimens at the common intersection point of unloading–reloading cycles in the tensile domain. It is shown, herein, that the CIP – which has traditionally been evaluated by extrapolation of the average compliance slopes of unloading–reloading cycles – can be precisely measured by raw experimental data, alone. The effects of negative inelastic strain accumulation to matrix cracking and an analysis of material damage with respect to the elastic behaviour of fibers are also discussed in the text.

2. Experimental

2.1. Materials and specimens

Cross-ply SiC/BMAS composite laminates were processed by AEA Technology (Harwell Ltd., United Kingdom) and provided in plate form, 3 mm thick. Silicon carbide grade “Tyranno” fibers (UBE Industries Ltd., Japan) were used to reinforce the glass–ceramic matrix. The 7 main steps in the composite manufacturing route were: (a) desizing of the SiC Tyranno fiber bundles in a furnace, (b) wetting the desized fibers in a slurry of the precursor glass frit, (c) winding the fibers on a mandrel and allowing to dry for 20 min, (d) cutting and manually arranging the fibers in layers for the preparation of prepreg sheets, (e) stacking the sheets in (0,90)_{4s} sequence, (f) burning the binder off and (g) hot pressing in a graphite die at ~1200 °C for 10 min. A final crystallization step involved heat treatment to ca 1300 °C.

It is known that during hot-pressing of SiC fiber-reinforced glass–ceramic matrix composites, the chemical reaction occurring between the fiber surface and the oxides of the matrix, results in the formation of a carbon-rich interphase layer [18,19]. This layer provides a weak fiber/matrix interfacial bond which – in combination with a brittle matrix – can result in fiber-bridged matrix cracks when the material is loaded in tension. The nominal elastic modulus and strength of the Tyranno fibers, as given by the manufacturer, are 190 GPa and 3.3 GPa respectively.

The composite plates were cut in a CNC vertical machining center to rectangular beams of dimensions $l \times w \times t = 105 \times 12 \times 3 \text{ mm}^3$ with the orientation of fibers in the external plies parallel to the loading axis (0°). Notches of various lengths were machined using a 300- μm thick diamond wafering blade (Model 5 LC Diamond Series, Buehler Co. Ltd., Lake Bluff, IL, USA). Notch-

to-width ratios (notched ligament fractions) of 0.35 and 0.2 were prepared to investigate the effect of notch length on properties. Un-notched and “dogbone” specimens were also prepared for static and cyclic loading tests. Sets of three specimens were prepared for each case.

Tensile testing at ambient temperature was performed under crosshead displacement control on an Instron 8800 servohydraulic test system (Illinois Tool Works, Glenview, IL, USA) equipped with a 100 kN load cell and hydraulic clamping grips. Strain was monitored via an external clip-on axial extensometer, gauge length 25 mm, equipped with knife-edge mounting legs. All specimens were tested without end-tabs and were gripped with a pressure of 4 MPa at an inter-grip distance of approximately 50 mm. Testing was conducted at a crosshead rate of 0.2 mm/min providing an initial strain rate of $4.0 \times 10^{-3} \text{ min}^{-1}$ within the effective gauge length.

Two AE sensors (Pico, PAC) were tape-mounted on the same side of the specimen as the clip-on extensometer, with a separation distance of 40 mm. Their broadband frequency response (50–800 kHz) enabled the acquisition of signals from various fracture mechanisms, while their small size allowed geometric location of the source events in the longitudinal axis of the specimen. The sampling rate was set to 5 MHz, the acquisition was conducted on a PCI-2 board of PAC, while threshold was set at 45 dB to exclude ambient noise. The sensor-free face of the specimen was monitored throughout testing by a thermography camera (CEDIP, MIW) with a cooled indium antimonide (InSb) detector (3–5 μm) and a focal plane array (FPA) with pixel format of 320 (H) \times 240 (V). The sensitivity of the IR camera is 20 mK and the frame rate 100 Hz. Fig. 1 demonstrates a typical arrangement of specimen and equipment (clip-on extensometer, AE sensors and IRT camera) during testing.

The unloading–reloading cycle algorithm was developed based on a theoretical 1% failure strain that is relevant for reinforced ceramics. The first unloading stage was set to commence at 10^{-3} strain and subsequent loops occurred with a strain step of 1.5×10^{-3} . All specimens were unloaded to full relaxation; in practice, reloading was triggered after zero load was attained upon unloading. Loading, unloading and reloading stages were performed with the same crosshead displacement rate of 0.2 mm/min.

3. Results and discussion

3.1. Material performance under cyclic tension

Typical cyclic tension curves for three DEN specimens of different notch-to-width ratios of the SiC/BMAS composite are shown in

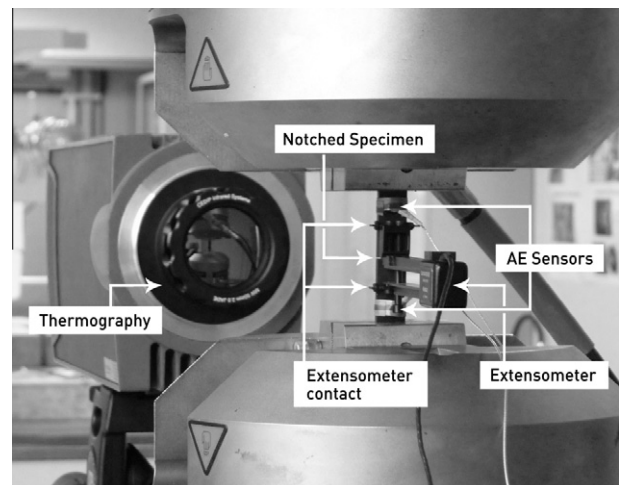


Fig. 1. Experimental arrangement for cyclic testing of DEN specimens with simultaneous AE and thermography monitoring.

Fig. 2. The response of the material in static tension is also included in the bottom graph of Fig. 2 as a dashed line. The tensile curves of the composites exhibited an initial linear part, followed by a regime of gradually decreasing tangent modulus to the curve. This softening is attributed to interfacial debonding and slipping between matrix and fiber in the area confined between neighboring matrix blocks. These blocks, interconnected through fiber bundles, are formed as a result of matrix cracks developing in planes perpendicular to the fibers' axis, initially within the 90° plies and subsequently also in the 0° plies. The decreasing average slope of unloading–reloading cycles, compatible with decreasing material stiffness, is also indicative of progressive damage in the matrix and interface.

For notched specimens, the second part of the curve was followed by the attainment of the maximum load and the material failed shortly after that; the associated curves showed minimal “tail” effect.

In the case of un-notched specimens, the tensile curves exhibited an additional, third, part of increased apparent stiffness and tangent modulus. As will be discussed also in a following section, within this regime interfacial debonding and matrix cracking have reached a saturated state, matrix load cannot increase further and fibers bear the global load. Material damage is not governed by the interface or matrix anymore, but by a mechanism of superior strength, namely load bearing by intact fibers, hence a macroscopic stiffening phenomenon is apparent, coupled with an almost linear stress–strain relationship. The envelope to the curve increases in stress until failure of the first fiber bundle leads to a decrease in V_f and, soon after, to the catastrophic failure of the composite. Such stiffening phenomena and linear stress–strain end-shapes in composite tensile curves, due to load-bearing fibers in a completely cracked matrix, have been reported in the past [20–22]. It should be noted that this third regime is totally absent in the tensile

curves of notched specimens, probably due to strain concentration gradients that rise in the vicinity of the notch root and induce premature fiber failure.

Based on the above argumentation, the slope of the final unloading cycle before failure (Fig. 2) must correspond to the purely elastic behavior of load-bearing fibers in the composite. This behavior can be approximated by a line of slope $\lambda E_f V_f$, where E_f is the Young's modulus of the fibers, V_f is the fiber volume fraction and λ is the non-unidirectional reinforcement correction factor, accounting only for fibers oriented in the direction of load application. The slope of the last unloading cycle, calculated as 52 GPa, is then equal to $\lambda E_f V_f$. Using $E_f = 190$ GPa and $\lambda = 0.5$ for biaxial reinforcement, the effective fiber volume fraction in the composite is calculated as 55%. The experimentally-established $\lambda E_f V_f$ line is included in all graphs of Fig. 2, as solid straight lines through the origin, to facilitate an analysis to follow.

One of the most prominent features in the stress–strain behavior of un-notched specimens was a precisely-well-defined CIP of unloading–reloading curves in the first quadrant of the stress–strain curve, at ca. 0.001 strain/90 MPa within the tensile domain, that is directly related to the axial residual stress state of the composite specimen. In [3,4], and [6], Steen, Camus and Mei determined the CIP by extrapolation of the compliance slopes of each reloading–unloading loop. In this manner, the compressive TRS of the fibers was established by the coordinates of the CIP that fell in the compression domain. By the same extrapolation method, Morscher calculated a tensile residual state of reinforcing SiC fibers in a silicon carbide matrix [23]. To the authors' knowledge, this is the first study to report a CIP that is precisely self-assembled in the tension domain, by raw unloading–reloading cycle data alone.

By comparison of the un-notched material response under static and cyclic tension (curves in the bottom graph of Fig. 2), an unambiguous overall strengthening is observed as a result of cyclic loading. Most interestingly, the pure tension curve perfectly intersects the CIP of unloading–reloading cycles of un-notched specimens at 0.3% strain. The overall shapes of the two curves were qualitatively comparable, with the previously explained “triple regime” behavior being apparent in both testing conditions. Quantitatively, at strains lower than the CIP, the material's response under pure tension appeared of comparable magnitude to that of cyclic loading. After the CIP, the tangent modulus to the pure tension curve decreased more rapidly than that of cyclic loading. This resulted in the debonding/softening regime of the pure tension curve commencing at lower stresses, however at the same strain level of 0.3% as in the cyclic tension case. Within the stiffening regime, which appeared at ca. 0.6% irrespectively of loading type, the tangent modulus decreased more rapidly in the pure tensile curves than in cyclic tension ones. The ultimate failure strain of ca. 0.85% was also common for the two tests, indicating that addition of unloading–reloading cycles does not essentially affect the maximum achievable deformation of the material. The overall effect of cyclic loading can be calculated as a 20% increase in attainable material stress. The above findings indicate that the mechanisms of saturated matrix cracking, softening due to interfacial debonding and stiffening due to load-bearing by intact fibers are not essentially triggered by the introduction of unloading–reloading cycles; but their magnitude is unambiguously strengthened by such testing conditions.

In all specimens, the shape of unloading and reloading loops during the initial couple of cycles was straight and the two lines were coincident. After that, loops exhibited hysteresis due to increasing friction between fiber and matrix at the progressively debonding interface. Hysteresis was also coupled with deviation from linearity of the unloading curve and introduction of positive curvature. It is believed that the shape of the loops is controlled by the sliding state and the frictional coefficient at the fiber–matrix

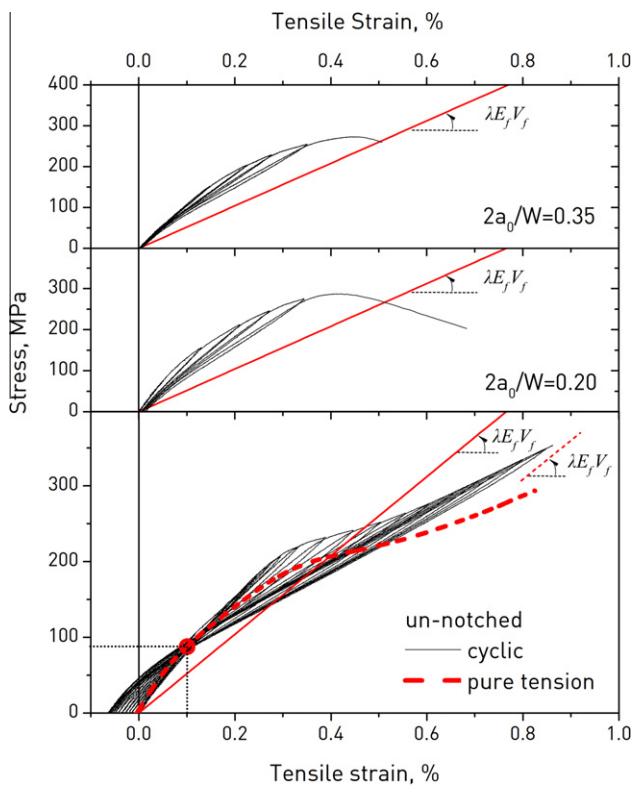


Fig. 2. Examples of tensile curves of the SiC/BMAS composite for varying notch-to-width ratios. (For interpretation of the references to color in this figure legend, the reader is referred to the web version of this article.)

interface. During the initial loading cycles both the matrix and the fibers can support the load through a high coefficient of friction, hence no sliding occurs. Further into loading, fiber sliding begins. Evans et al. [1] have explained the shape of hysteresis loops in the fatigue behavior of CMC upon the mechanism of crack closure. According to their theory unloading curves of positive curvatures are related to composites with small debond energies (SDE) while those with large debond energies (LDE) have a linear unloading curve. The extent of hysteresis appeared to increase with cycle count within the debonding regime. In the case of un-notched specimens, the hysteresis effect disappeared towards the final cycles because, as already discussed, within the final regime, matrix cracking and debonding – hence also friction – have completed and any load increment is carried by the intact fiber population alone.

After the end of the tests, failed specimens had not separated completely and could be removed from the grips in one piece indicating that bridging fibers had failed within the matrix environment and had partially pulled-out before removal of the specimens from the grips, at positive load values of the order of a few tens of Newtons. The finding that bridging fibers did not fail between the crack flanks, where stresses are maximum, but within the matrix, can be rationalized upon the tampering effect that sliding across the debonded interface has on the surface flaw distribution of fibers, that controls fiber failure [24]. On the other hand, the existence of the pull-out mechanism is a standalone proof of a weak interfacial bond that may have been additionally weakened by cycling loading. The post-mortem condition of the notched ligaments of tested specimens was examined under a Leica MZ-75 Stereoscope. As seen in Fig. 3, the crack propagation in the glass-ceramic matrix involved several deflection stages while fiber bridging was extensive throughout the whole ligament.

The fracture strength of the composite decreased with increasing notch length. Un-notched specimens had an average strength of 355 MPa whereas specimens with notch-to-width ratios of 0.35 and 0.2 exhibited average strengths of 270 and 280 MPa, respectively. The initial moduli of the composite, measured over a 25 mm gauge length, decreased with increasing notch length; average values of 108, 119 and 151 GPa were calculated for specimens with notch-to-width ratios of 0.35, 0.2 and 0. The theoretically-expected value for the composite's elastic modulus, based on the rule of mixtures for $E_f = 190$ GPa, $E_m = 120$ GPa [25], $\lambda = 0.5$ and the experimentally determined value of $V_f = 0.55$, is $E_c = 106$ GPa. The divergence observed between the theoretical and experimental modulus values is a result of the effect of axial TRS state of material. Furthermore, the dependency of modulus on notch length can be attributed to the finite dimensions of the gauge length compared to the stress concentration region. These aspects are further explained in the following section.

3.2. Residual stresses

According to Steen [3], scattered tensile curves of the same composite occurring as a result of inter-specimen axial residual stress variations, can be brought to coincidence by application of a translation vector in the stress-strain plane. The origin of the assembled "mastercurve" corresponds to the CIP of the average regression lines to consecutive unloading-reloading cycles and directly relates to the axial residual stress state of fibers in the composite as such: The stress co-ordinate of the CIP is equal to the average axial residual stress in the fibers multiplied by their volume fraction, whereas the strain co-ordinate corresponds to the axial residual strain in the fibers averaged over the gauge length. Applying this argumentation to the ceramic matrix composite of this study, the axial residual stress and strain of the SiC fibers in the BMAS matrix can be calculated directly from the coordinates of the self-assembled CIP, as 163 MPa and 0.1% respectively. The

tensile nature of these residuals indicates that, during cooling of the composite from manufacturing to ambient temperature, axial fiber shrinkage was restricted by the surrounding matrix. This requirement is only satisfied by a matrix of a lower CTE than the reinforcing fibers. Indeed, the CTE of the BMAS matrix is in the range of $2-3 \times 10^{-6} \text{ K}^{-1}$ [26], whereas SiC-Tyranno fibers have a CTE of $4-4.5 \times 10^{-6} \text{ K}^{-1}$ according to the manufacturer. The theoretical value of axial TRS in a non-cracked matrix, in a composite with ideal interface bond, can be estimated by [6]:

$$\sigma_r^m = E_m \frac{\lambda E_f V_f}{\lambda E_f V_f + E_m V_m} (a_f - a_m)(T_o - T_p) \quad (1)$$

where α_f and α_m are the linear CTE of the fiber and matrix, respectively and T_o and T_p are the operation and processing temperatures, respectively. Using the aforementioned values for E_f , E_m , λ and V_f , and $\alpha_f = 4.5 \times 10^{-6} \text{ K}^{-1}$, $\alpha_m = 2.5 \times 10^{-6} \text{ K}^{-1}$, $T_o = 298 \text{ K}$ and $T_p = 1573 \text{ K}$, the expected axial residual stress in the non-cracked matrix is compressive at 150 MPa. The corresponding axial residual stress on the fibers should then be on opposite sign and equal magnitude, hence tensile at 150 MPa. This theoretical TRS value is 8% less than the experimentally measured TRS of 163 MPa. This discrepancy is not unreasonable considering the simplicity of Eq. (1) and the assumption of non-cracked matrix.

By application of the translation vector approach to the composite under investigation, the tensile curve can be shifted in the stress-strain plane so that the CIP defining the residual state of the composite, is brought to coincidence with the origin. This has the result depicted in Fig. 4. The initial composite modulus, calculated through the new origin, is now 104 GPa, close to the value of the notched specimens (residual-free) and compares favorably with the theoretical expectation based on the rule of mixtures, 106 GPa. This finding demonstrates the significant effect of the TRS state on the material properties that are calculated through mechanical testing data.

It should be added that *radial* residual stresses also develop during material processing. These stresses influence the degree of load transfer between the fibers and the matrix across the interface, hence they affect the amount of frictional energy dissipation during interfacial sliding, which is represented by the area of the hysteresis loops during cycling loading. However this area does not affect the envelope tensile behavior and the calculated elastic constants of the material.

It should be recalled that the tensile curves of double-edge notched specimens did not exhibit a CIP, as seen in Fig. 2. This finding signifies that the TRS may be relieved in notched specimens due to (positive) stress concentration gradients acting in the neighborhood of the notch root, that cancel the negative TRS state of the matrix. For a machined notch radius of 125 μm , (Fig. 3), the stress around the notch can theoretically magnify up to 6–8 times of the macroscopically applied value, for specimens with 0.2 and 0.35 notch-to-width ratios. If, at the conventional yield strength of the material, this stress concentration spans a region that is equal to the notch length -as the classical Irwin plastic zone approach predicts- then the remaining unaffected ligament may be of insufficient dimensions for its TRS to affect the overall mechanical behavior.

3.3. Matrix cracking and negative strain accumulation

The elastic behavior of fibers in the composite (line of slope $\lambda E_f V_f = 52$ GPa) is included in the tensile curves of Fig. 2. The point of intersection of the $\lambda E_f V_f$ line with a tensile curve defines a fully-saturated matrix cracking state where fibers in the loading direction are completely bridged by the transverse saturated matrix cracks [3]. In this context, tensile data located above the $\lambda E_f V_f$ line

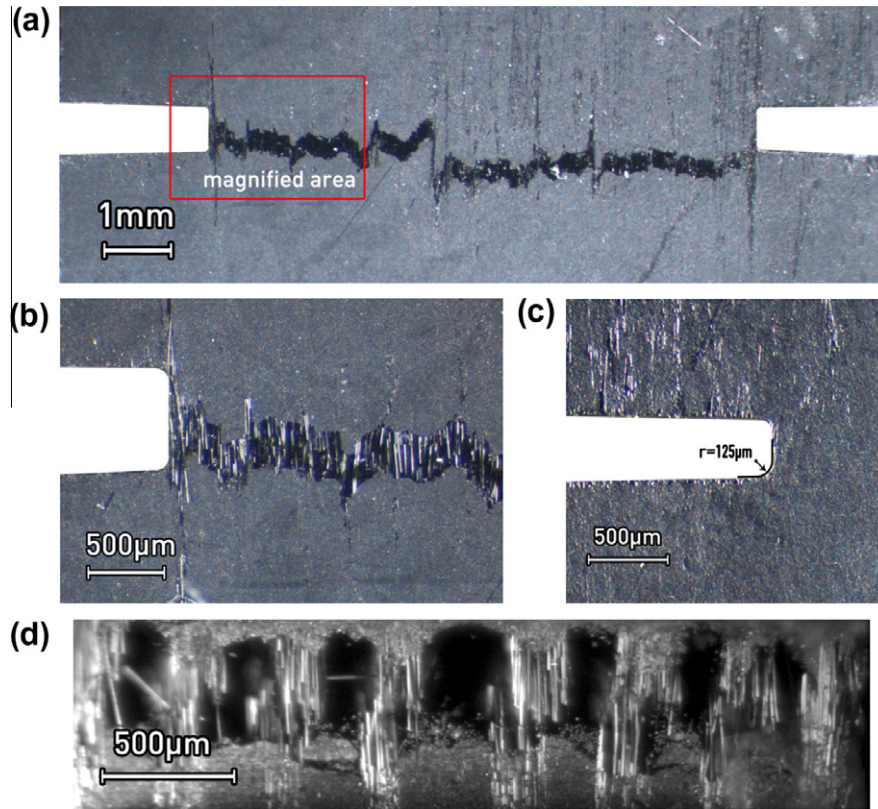


Fig. 3. Optical microscopy imaging of the SiC/MAS specimen. (a) Post-mortem condition of the notched ligament of the DEN specimen demonstrating the dominant macro-crack and crack deflection path. (b) Magnification of the notch root region and large scale bridging phenomena. (c) Notch root and radius before test. (d) Post-mortem image of the transverse cracking path. (For interpretation of the references to color in this figure legend, the reader is referred to the web version of this article.)

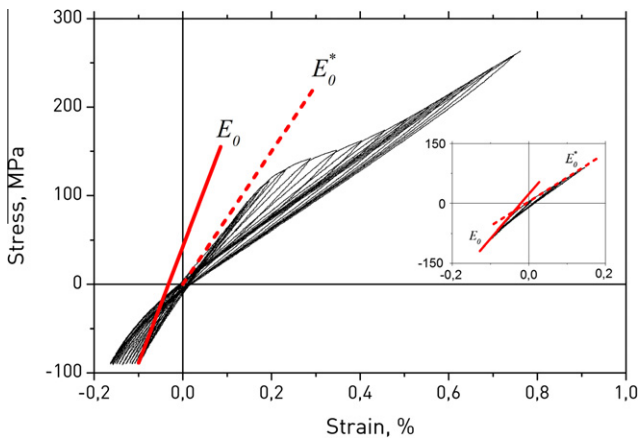


Fig. 4. Effect of translated tensile curve of un-notched specimen on calculated elastic modulus. (For interpretation of the references to color in this figure legend, the reader is referred to the web version of this article.)

are associated with large nonlinear phenomena due to time-dependent matrix cracking. Below the $\lambda E_f V_f$ line, lies the regime of global load sharing by intact fibers and fiber bundles in a completely cracked matrix that results in the macroscopic “stiffening” phenomenon and the linear stress–strain relationship toward the end of the curve. As shown in Fig. 2, the curves of notched specimens, including all cycle loading data, are located above the $\lambda E_f V_f$ line and the line intersects the tensile curve essentially at failure. This observation indicates that a fully-saturated matrix cracking state is a fatal condition for the notched specimens. In the presence of notches, the material cannot sustain the bridging phenomenon.

In the case of un-notched specimens, a totally different behavior is noted: the elastic line crosses the curve towards the end of the debonding regime. In absence of any internal stress concentration gradients, the matrix crack saturation stress, 250 MPa, is fully sustained by the composite and the “stiffening” regime appears.

All specimens tested in cyclic loading exhibited inelastic strain accumulation upon unloading. Inelastic strain, calculated as the strain offset at zero load at the onset of reloading, is plotted as a function of cycle stress (stress at the onset of unloading) for different notch-to-width ratios in Fig. 5. Notched specimens exhibited a small degree of positive inelastic strain accumulation with values increasing with increasing notch length. The scenario changed dramatically in the un-notched specimens where inelastic strain was of negative sign and reached a maximum value that was more than 4 times greater than of notched specimens. For un-notched specimens, it was also observed that inelastic strain increased with cycle count and attained a plateau value in the final cycles where matrix cracking was saturated. This finding implies that inelastic strain is related to matrix cracks, most possibly through the mechanical impediment of complete crack closure due to fiber roughness and/or contact between opposing faces micro-crack slightly moved from their original positions during unloading–reloading. This explanation is further supported by analysis of the hysteresis loops that showed an apparent increase in stiffness towards relaxation, i.e. an increase in the tangent modulus of the unloading curve at the lower ends of the loops.

The origins of negative strain accumulation are explained in the following. When the residual stress in the matrix is compressive (tensile in the fibers), relief of TRS during loading causes an expansion of the matrix blocks and a contraction of fibers bridging the cracks. This results in a certain degree of matrix crack closure. If the residual stresses were of opposite sign, the matrix blocks

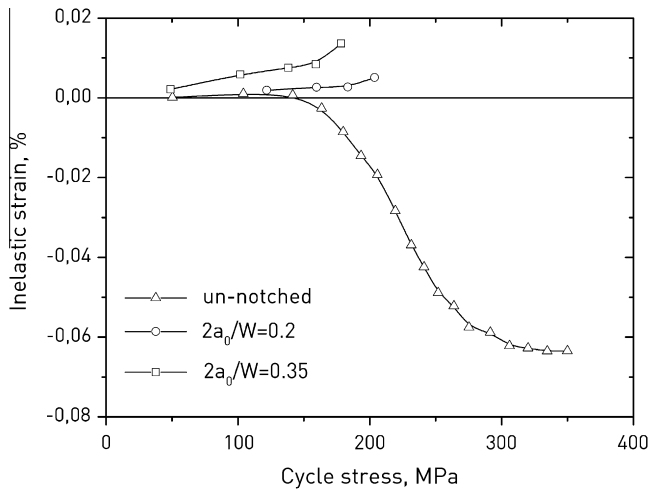


Fig. 5. Cumulative inelastic strain as a function of cycle stress for varying notch-to-width ratios of the SiC/BMAS composite. Solid lines connecting experimental points are spline regressions to the data.

would tend to contract and fibers would expand, thus matrix crack opening would increase. When the matrix is under residual compression, it is possible that matrix cracks can be sufficiently closed for the TRS relief to not allow expansion of the matrix blocks and contraction of fibers. This leads to a tangent unloading modulus equal to the modulus of the previous loading. As a result, the unloading curve can shift to the left of the previous loading curve and negative strain accumulation is observed. At reloading, matrix cracks are closed and the tangent reloading modulus is equal to the modulus of the previous unloading. This makes the reloading curve lie below the previous unloading curve. The effect expands self-similarly with increasing maximum stress in the unloading–reloading cycles.

3.4. Acoustic emission monitoring

Acoustic emission is the result of irreversible processes: mainly crack propagation, constituent failure, and changes in the microstructure. Any fracture incident releases energy in the form of stress waves and is captured by piezoelectric sensors on the surface of the material [27]. The number of acquired signals is connected to the number of active sources while the location of the source event can be calculated by the time delay between the recording of each signal by different sensors [28]. Analysis of acoustic signals enhanced the understanding of the fracture mechanisms and their sequence throughout the failure process of the CMC under investigation. Fig. 6 indicatively shows the strain and cumulative AE activity histories for specimens with notch-to-width ratios of 0.2 (a) and 0.35 (b). It can be seen that each successive loading step induced more AE hits since the maximum strain increased and damage accumulated. It is also obvious that the rate of incoming hits was maximized when strain had almost attained the maximum value for each cycle. After the peak strain, the rate of AE acquisition dropped to approximately one third until the next reloading stress that exceed the previous cyclic peak stress, as seen in Fig. 6b. A similar behavior has been reported by Mei et al. in [29] for a carbon-fiber-reinforced SiC matrix composite (C/SiC) subjected to thermal cycling between 700 and 1200 °C. For the specimen with notch-to-width ratio of 0.35, the acquisition of AE continued even after failure since significant acoustic activity was still being recorded. As discussed in the following, the activity captured at times higher than 300 s showed a distinct population of events that can be attributed to fiber sliding and pull-out.

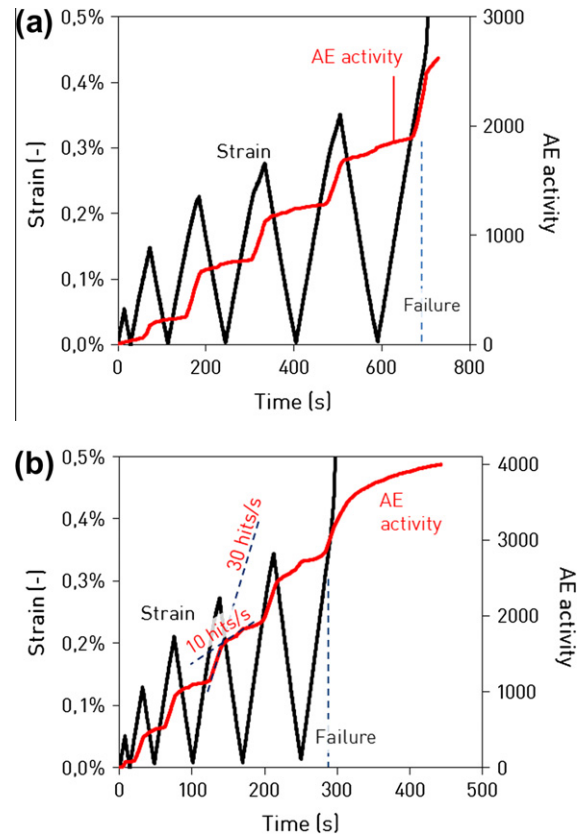


Fig. 6. Strain and time histories for specimens with notch-to-width ratios of (a) 0.2, and (b) 0.35. (For interpretation of the references to color in this figure legend, the reader is referred to the web version of this article.)

If we were to concentrate on events only, (signals that were simultaneously recorded by both sensors and attributed to the same source incident), interesting trends arise as to their location. Fig. 7a shows the location of events and the associated time instances for an un-notched specimen. The total number of events is below 100 and their location exhibits a wide distribution in the whole measured length of the specimen. For the notched specimens, the events are reasonably located in the center zone of the specimen (see Fig. 7b, location 20 mm from the first sensor). A percentage of 56% of the total number of events was included in a zone of ± 2.5 mm from the center, a result clearly attributed to the presence of the notch that marks the fracture process zone. Due to the sensitivity that the notch brings into the specimen, the number of events is quite high (more than 400) compared to the case of un-notched specimen. This shows the ability of AE to distinguish and locate accurately events coming from certain discontinuities even at close separation distances of 40 mm.

It is quite interesting to recall that the specimens were not separated after failure. As was discussed earlier, this is attributed to the failure of fibers within the matrix and not necessarily between the macroscopic crack flanks. The same effect was captured also in the AE data: Even after termination of the loading procedure and the macroscopic failure of the specimen at approximately 300 s, AE activity was still being recorded, with a very distinct new cluster of signals emerging at peak frequencies between 400 and 500 kHz, as seen in Fig. 8. While other classes ranging from below 100 kHz to 400 kHz were active since the beginning of the test, the specific cluster is essentially activated by failure itself, as signals of this level of peak frequency were rare before. Since after failure the external load has dropped to practically zero, the only plausible explanation for the recorded AE activity is the friction produced

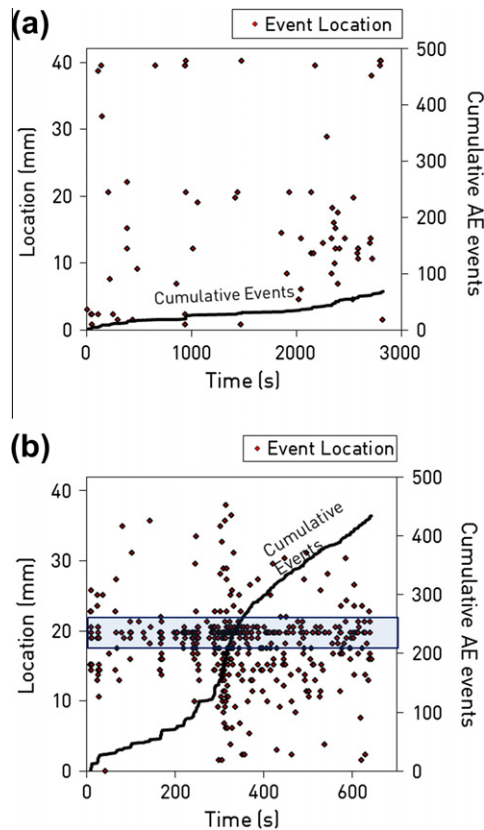


Fig. 7. Location and time histories of events for specimen with (a) $2a/w = 0$ and (b) $2a/w = 0.35$. (For interpretation of the references to color in this figure legend, the reader is referred to the web version of this article.)

during sliding of the failed fibers' surfaces as they pull outside the matrix. This hypothesis is further supported by the continuously decreasing rate of AE signals, attributed to more and more fibers gradually disengaging from the matrix environment.

It should be stressed that the thin specimen geometry certainly induces dispersion effects on the propagating waveforms and therefore, frequency as well as any other features received by the sensors may well be different compared to their original content. In the present case, although this influence is certainly active, the short gauge length enables such preliminary conclusions to be

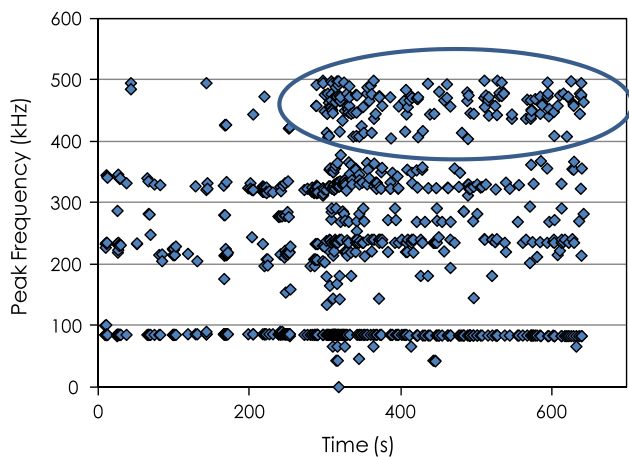


Fig. 8. Peak frequency for all the events monitored during fracture of specimen 2. (For interpretation of the references to color in this figure legend, the reader is referred to the web version of this article.)

drawn; however, for longer propagation distances, determination of distinct classes would be more troublesome.

3.5. Infrared thermography monitoring

IRT was used to capture valuable information concerning the location and evolution of damage in the CMC under investigation. Fig. 9 focuses on the damage sequence captured via IRT within the last reloading cycle of the specimen with notch-to-width ratio of 0.2, upto failure. Thermographs a–h in Fig. 9 show the magnitude of damage occurring within the material at select critical instances within this cycle. Time and strain associated with each thermography instance are correlated to the thermographs by dashed lines; time in sec is also indicated in the thermographs' label.

Fig. 9a demonstrates the baseline thermal fingerprint of the composite specimen prior to the commencement of catastrophic fracture, with no obvious temperature variations evident on the specimen's surface. Damage commenced 5 s within the last reloading cycle, at 600 s, and is indicated by a red¹ circle in Fig. 9b. Notwithstanding the fact that this instance falls within an apparently "linear" regime, it should be reminded that, at this loading stage, the material had already undergone 4 unloading–reloading cycles and extensive interfacial damage had already occurred. Initiation of fiber failure appeared at 680 s on the left side of the specimens, as clearly captured in Fig. 9c (green cycle) and is directly associated with the macroscopically observed decrease in modulus, that is due to the decrease in V_f . Fiber failure progressed in a stable manner within the next 10 s, with damage gradually accumulating over half of the notched ligament, under the global load sharing principle, as evident in Fig. 9d and e. It appears that, once ca. 50% of fibers had failed, their remaining population was not sufficient to withstand the macroscopically applied load, and spontaneous fiber failure was triggered. Hence, within the next 300 ms (Fig. 9f) the remaining intact fibers failed massively within the matrix environment. This observation validates our previous finding that notched specimens failed soon after the attainment of the maximum load and did not exhibit a final stiffening regime. Once fiber failure had spanned the whole bridged ligament, the magnitude of damage, as captured by IRT, appeared to gradually fade out symmetrically from both notch roots (Fig. 9g). This "fade-out" is believed to be associated with the contraction of failed fiber ends within the matrix environment, prior to the initiation of the pull-out. As shown in the thermograph of Fig. 9h, no significant new damage developed in the material prior to load relaxation.

4. Conclusions

The mechanical performance of a SiC_f/BMAS ceramic matrix composite was investigated under tensile loading in view of the effects of the thermal residual stress state, presence of notches and imposition of unloading–reloading cycles during testing. It was found that:

- (1) Material performance was consistent with a triple regime scheme consisting of an initial elastic regime, a softening regime associated with decreased tangent modulus due to progressive interfacial damage, and a final regime of increased tangent modulus and stiffness comparable to that of intact fibers stretched in air. Cyclic loading resulted in an increase by 20% in the sustainable material stress. IRT showed that ultimate material failure was controlled by

¹ For interpretation of color in Fig. 9, the reader is referred to the web version of this article.

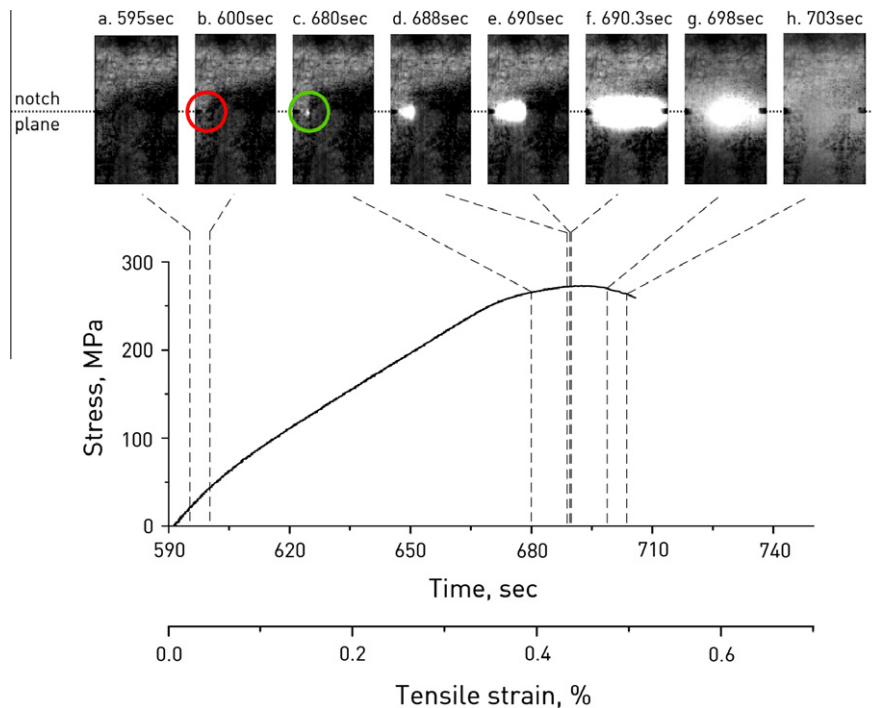


Fig. 9. Thermographic imprinting of damage evolution during the ultimate reloading stage of a notched SiC/BMAS composite. (For interpretation of the references to color in this figure legend, the reader is referred to the web version of this article.)

the intact fiber population. Material response and matrix cracking was successfully assessed by means of the elastic line of fibers in the composite.

- (2) In the presence of notches, the stiffening regime was truncated as a result of stress concentration gradients inducing premature fiber failure at the vicinity of the notch root. Double-edge-notch specimens failed spontaneously shortly after a saturated matrix cracking state was achieved, as validated also by IRT results. Scattered elastic moduli values observed in specimens of different notch lengths were reconciled by application of a translation vector approach in the stress-strain plane.
- (3) The thermal residual stress of fibers was calculated directly from the coordinates of a precisely well-defined common intersection point of cyclic data in the tension domain, as 163 MPa and compared favorably with the prediction of a popular theoretical TRS model. As a result of the established TRS, negative strain accumulates in the un-notched material during unloading because matrix cracks can close sufficiently to prohibit fiber contraction.
- (4) Acoustic emission parameters exhibited sensitivity to the stress conditions by the cumulative activity, frequency descriptors as well as geometric location of source cracks. Fiber pull-out induced a distinct cluster of acoustic emission events of characteristic peak frequency of 400–500 kHz.

References

- [1] Evans AG, Domergue JM, Vagaggini E. Methodology for relating the tensile constitutive behavior of ceramic-matrix composites to constituent properties. *J Am Ceram Soc* 1994;77(6):1425–35.
- [2] Domergue JM, Vagaggini E, Evans AG. Relationships between hysteresis measurements and the constituent properties of ceramic-matrix composites. 2. Experimental studies on unidirectional materials. *J Am Ceram Soc* 1995;78(10):2721–31.
- [3] Steen M. Tensile mastercurve of ceramic matrix composites: significance and implications for modelling. *Mater Sci Eng A-Struct* 1998;250(2):241–8.
- [4] Camus G, Guillaumat L, Baste S. Development of damage in a 2D woven C/SiC composite under mechanical loading. 1. Mechanical characterization. *Compos Sci Technol* 1996;56(12):1363–72.
- [5] Mei H, Cheng LF. Comparison of the mechanical hysteresis of carbon/ceramic-matrix composites with different fiber preforms. *Carbon* 2009;47(4):1034–42.
- [6] Mei H. Measurement and calculation of thermal residual stress in fiber reinforced ceramic matrix composites. *Compos Sci Technol* 2008;68(15–16):3285–92.
- [7] Amami S, Lemaitre C, Laksimi A, Benmedakhene S. Characterization by acoustic emission and electrochemical impedance spectroscopy of the cathodic disbonding of Zn coating. *Corros Sci* 2010;52(5):1705–10.
- [8] Scholey JJ, Wilcox PD, Wisnom MR, Friswell MI. Quantitative experimental measurements of matrix cracking and delamination using acoustic emission. *Compos Part A—Appl Sci* 2010;41(5):612–23.
- [9] Aggelis DG, Barkoula NM, Matikas TE, Paipetis AS. Acoustic emission monitoring of degradation of cross ply laminates. *J Acoust Soc Am* 2010;127(6):EI246–51.
- [10] Aggelis DG, Kordatos EZ, Soulioti DV, Matikas TE. Combined use of thermography and ultrasound for the characterization of subsurface cracks in concrete. *Constr Build Mater* 2010;24(10):1888–97.
- [11] Aggelis DG, Kordatos EZ, Strantza M, Soulioti DV, Matikas TE. NDT approach for characterization of subsurface cracks in concrete. *Constr Build Mater* 2011;25(7):3089–97.
- [12] Plekhov O, Pain-Luc T, Saintier N, Uvarov S, Naimark O. Fatigue crack initiation and growth in a 35CrMo4 steel investigated by infrared thermography. *Fatigue Fract Eng M* 2005;28(1–2):169–78.
- [13] Kordatos EZ, Aggelis DG, Matikas TE. Monitoring mechanical damage in structural materials using complimentary NDE techniques based on thermography and acoustic emission. *Composites Part B—Eng* 2012.
- [14] Myriounis DP, Kordatos EZ, Hasan ST, Matikas TE. Crack-tip stress field and fatigue crack growth monitoring using infrared lock-in thermography in A359/SiCp composites. *Strain* 2011;47:E619–27.
- [15] Kordatos EZ, Matikas TE. Developing damage metrics for metallic structures undergoing fatigue using real-time thermographic evaluation. In: *Proceedings of SPIE*, vol. 79822011.
- [16] Maldague XPV. Introduction to NDT by active infrared thermography. *Mater Eval* 2002;60(9):1060–73.
- [17] Mei H, Cheng LF. Stress-dependence and time-dependence of the post-fatigue tensile behavior of carbon fiber reinforced SiC matrix composites. *Compos Sci Technol* 2011;71(11):1404–9.
- [18] Cooper RF, Chyung K. Structure and chemistry of fiber matrix interfaces in silicon-carbide fiber-reinforced glass ceramic composites – an electron-microscopy study. *J Mater Sci* 1987;22(9):3148–60.
- [19] Benson PM, Spear KE, Pantano, GC. Interfacial characterisation of glass matrix/Nicalon SiC fiber composites: a thermodynamic approach. *Ceram Eng Sci Proc* 1988;9:663–70.

- [20] Wang M, Laird C. Characterization of microstructure and tensile behavior of a cross-woven C–SiC composite. *Acta Mater* 1996;44(4):1371–87.
- [21] Wang MD, Laird C. Tension–tension fatigue of a cross-woven C/SiC composite. *Mater Sci Eng A-Struct* 1997;230(1–2):171–82.
- [22] Cady C, Heredia FE, Evans AG. Inplane mechanical-properties of several ceramic–matrix composites. *J Am Ceram Soc* 1995;78(8):2065–78.
- [23] Morscher GN, Singh M, Kiser JD, Freedman M, Bhatt R. Modeling stress-dependent matrix cracking and stress–strain behavior in 2D woven SiC fiber reinforced CVSiC composites. *Compos Sci Technol* 2007;67(6):1009–17.
- [24] Dassios KG, Galiotis C. Direct measurement of fiber bridging in notched glass–ceramic–matrix composites. *J Mater Res* 2006;21(5):1150–60.
- [25] Widjaja S. Determination of creep-induced residual stress in fiber-reinforced glass–ceramic matrix composites by X-ray diffraction. *Mater Charact* 2001;47(1):47–54.
- [26] Jais US, Lee WE, James PF. Crystallization of barium osumilite glass. *J Am Ceram Soc* 1999;82(11):3200–8.
- [27] Grosse CU. *Acoustic emission testing: basics for research – applications in civil engineering*. New York: Springer; 2008.
- [28] Schechinger B, Vogel T. Acoustic emission for monitoring a reinforced concrete beam subject to four-point-bending. *Constr Build Mater* 2007;21(3):483–90.
- [29] Mei H, Cheng LF, Zhang LT, Fang P, Meng ZX, Liu CD. Real-time monitoring of thermal cycling damage in ceramic matrix composites under a constant stress. *J Am Ceram Soc* 2007;90(7):2135–42.